Published in final edited form as:
Eur J Radiol. 2007 December ; 64(3): 335–344.

Hyperpolarized ^{129}Xe MRI: A Viable Functional Lung Imaging Modality?

Samuel Patz, PhD[1,2], **F. William Hersman, PhD**[3], **Iga Muradian, PhD**[2], **Mirko I. Hrovat, PhD**[1,4], **Iulian C. Ruset, PhD**[3], **Stephen Ketel, BS**[3], **Francine Jacobson, MD**[2], **George P. Topulos, MD**[4], **Hiroto Hatabu, MD, PhD**[1,2], and **James P. Butler, PhD**[1,6]

1 *Center for Pulmonary Functional Imaging, Brigham and Women's Hospital 221 Longwood Avenue, Boston, MA 02115*

2 *Department of Radiology, Brigham and Women's Hospital 75 Francis Street, Boston, MA 02115*

3 *Department of Physics, University of New Hampshire 131 Main Street, Nesmith Hall, Durham, NH 03824*

4 *Mirtech, Inc., 452 Ash Street, Brockton, MA 02301*

5 *Department of Anesthesiology, Brigham and Women's Hospital 75 Francis Street, Boston, MA 02115*

6 *Department of Environmental Health, Harvard School of Public Health 665 Huntington Avenue, Boston, MA 02115*

Abstract

The majority of researchers investigating hyperpolarized gas MRI as a candidate functional lung imaging modality have used ^{3}He as their imaging agent of choice rather than ^{129}Xe. This preference has been predominantly due to, ^{3}He providing stronger signals due to higher levels of polarization and higher gyromagnetic ratio, as well as its being easily available to more researchers due to availability of polarizers (USA) or ease of gas transport (Europe). Most researchers agree, however, that hyperpolarized ^{129}Xe will ultimately emerge as the imaging agent of choice due to its unlimited supply in nature and its falling cost. Our recent polarizer technology delivers vast improvements in hyperpolarized ^{129}Xe output. Using this polarizer, we have demonstrated the unique property of xenon to measure alveolar surface area noninvasively. In this article, we describe our human protocols and their safety, and our results for the measurement of the partial pressure of pulmonary oxygen (pO_2) by observation of ^{129}Xe signal decay. We note that the measurement of pO_2 by observation of ^{129}Xe signal decay is more complex than that for ^{3}He because of an additional signal loss mechanism due to interphase diffusion of ^{129}Xe from alveolar gas spaces to septal tissue. This results in measurements of an equivalent pO_2 that accounts for both traditional T_1 decay from pO_2 and that from interphase diffusion. We also provide an update on new technological advancements that form the foundation for an improved compact design polarizer as well as improvements that provide another order-of-magnitude scale-up in xenon polarizer output.

Keywords

hyperpolarized xenon; ^{129}Xe; lung imaging; surface area per unit volume; S/V; XTC; single breath XTC; SB-XTC; CSSR

Corresponding Author: Samuel Patz, PhD Department of Radiology, Center for Pulmonary Functional Imaging Brigham and Women's Hospital 221 Longwood Avenue Boston, MA 02115 Telephone: 617-278-0616 FAX: 617-278-0610 Email: patz@bwh.harvard.edu.

Introduction

Recognition of the value of hyperpolarized noble gases in performing nuclear magnetic resonance imaging has lead to research seeking the best methods for their production in large quantities. A foremost method is Spin Exchange Optical Pumping (SEOP). Much of the fundamental science of SEOP performed through the 1980s and early 90s was a product of Will Happer's group at Princeton. Due to his reputation in this area, he was approached by xenon spectroscopists Balamore and Albert from Stony Brook, who were seeking stronger signals for their studies of biochemical mechanisms of anesthesia. Their collaboration led to the recognition that hyperpolarized gases could be produced in large quantities, breathed, and imaged *in vivo*. Hyperpolarized noble gas imaging as well as some key elements of their device to produce hyperpolarized xenon was patented in the US. In 1996, Magnetic Imaging Technologies Inc. (MITI) was founded as a spin-off company from Happer's group to pursue the technology.

MITI continued technical refinement, produced and sold a few polarizers, and began collaborating with academics to develop imaging strategies. In 1999 MITI was bought by Nycomed Amersham, who began the process to seek regulatory approval. While they applied for hyperpolarized noble gases to be classified by the FDA as a device, instead these gases were classified as drugs. The projected expense required for human trials leading to regulatory approval mushroomed.

Two gases, ^{3}He and ^{129}Xe, can be hyperpolarized by SEOP. This process uses circularly polarized laser light tuned to an absorption line in rubidium to polarize rubidium vapor. Collisions between the rubidium atoms and the noble gas atoms transfer the polarization from the rubidium electrons to the noble gas nuclei. Thus, the polarized rubidium transfers its polarization to the noble gas, a phenomenon known as spin exchange, resulting in the hyperpolarized noble gas.

The technology for achieving high polarizations with ^{3}He had been a focus of Happer's group due to its applications in fundamental high-energy physics: consequently, liter quantities of > 35% polarized ^{3}He were routinely achievable. In contrast, however, liter quantities of xenon could be produced with polarizations typically less than 5-7%. This is largely because xenon poses an additional challenge: the xenon electrons usually depolarize the rubidium electrons before the rubidium electrons can polarize the xenon nucleus. Xenon polarization has low intrinsic photon efficiency.

Nycomed Amersham decided to concentrate their resources on the FDA approval of hyperpolarized helium imaging. ^{3}He offers a magnetic moment three times greater than ^{129}Xe and its polarization was five to ten times higher, yielding a signal strength advantage of up to 30.

In spring of 2004, General Electric acquired Amersham Health. To the best of our knowledge, GE has not pursued further advances in polarizer technology. In addition, GE recently announced [1] that they are vigorously pursuing hyperpolarized ^{13}C and are funding a pilot project at Duke University for ^{129}Xe. They announced that they are not pursuing commercial applications of ^{3}He.

Meanwhile, Hersman, a member of our group, had been building a technology development program to produce polarized helium cells to serve as particle beam targets for nuclear physics experiments. In 1997, after learning of the need for better methods to polarize xenon, he conceived of the counter-flow method and invented the counter-flow xenon polarizer. The University of New Hampshire team achieved a technological breakthrough in 2004:

Magnetization output, the product of polarization times the production rate, exceeded the output of the commercial Amersham polarizer by a factor of fifty, and exceeded that of the world's best polarizer, a scaled-up version of the Amersham polarizer developed at the National High Magnetic Field Laboratory (NHMFL), Tallahassee, FL, by a factor of ten to twenty. (See Fig. 1) [2,3].

Method: counter-current polarization

The counter-flow polarizer (Fig. 2) makes use of a main operating principle and two auxiliary supporting ideas, enabling a new regime of operation. The main principle is to flow the mixed gases along a long reaction chamber towards a laser beam emanating from the opposite direction. The gases are initially illuminated with the attenuated beam, achieving some degree of polarization. Near the end of the process, however, when gases are highly polarized, they are subjected to the most intense laser light to assure 100% rubidium polarization and raise the xenon polarization still further. This “counter-current” principle is also used in efficient heat exchangers.

The first auxiliary idea is to saturate the flowing gases with rubidium in a preparatory chamber outside the laser polarization region. This assures homogeneous saturation of the gases to a well-defined rubidium density (dependent on thermal bath temperature) essentially independent of flow velocity and laser power. The Princeton and NHMFL designs have the rubidium droplets in the polarization chamber. Higher flow rates result in incomplete saturation of the flowing gases with rubidium. Higher laser intensity results in a non-linear runaway condition, in which laser power absorption heated the gas vaporizing additional rubidium, which in turn increases laser absorption. Higher laser intensity in our system actually reduces rubidium density (higher temperature at constant partial pressure), maintaining stability.

The second auxiliary idea is to extract the rubidium in the presence of the polarizing light. By bringing the mixed flowing gases into contact with a cold surface in the presence of the laser light, the rubidium remains polarized, continuing to transfer polarization to the xenon, until it is extracted. The Princeton system exhausts mixed gases from the chamber still saturated with rubidium. If we employed that strategy, our rubidium would quickly lose its polarization and begin to depolarize the xenon.

The new operating regime enabled by these advances is high gas flow velocity, low gas pressure, and very low xenon partial pressure. The key benefit to low xenon partial pressure is the resulting ability to maintain high rubidium polarization with the laser. High xenon partial pressure leads to rapid rubidium depolarization. Of course, low xenon partial pressure then requires higher flow rates to polarize the same quantity of xenon.

The key benefit to low total gas pressure is the increase in polarization transfer from rubidium to xenon. Rubidium transfers polarization to xenon by two distinct processes: instantaneous binary collisions and formation of van der Waals molecules. Spin exchange by molecule formation has much higher probability if the molecule is not broken up by a subsequent collision, and therefore dominates at low pressures. We are able to achieve almost an order of magnitude increase in spin exchange rate and flow at much higher velocities.

Low pressure, however, can reduce the efficiency of extracting the laser light by the rubidium. Most polarizers require higher pressure to pressure-broaden the rubidium absorption spectral line. We achieved efficient laser absorption by increasing the length of the cell by a factor of ten, from a previous maximum length of 20 cm to almost two meters. These combined improvements provide liter quantities of xenon polarized up to and exceeding 50%, allowing high-quality human MR imaging protocols for the first time.

Progress towards a compact automated clinical polarizer

Hersman and his team have continued to identify paths for dramatically improving performance. In 2004 he founded Xemed LLC, with the initial purpose of refining technologies invented by his group at the University of New Hampshire (UNH), and with the long term goal of commercializing hyperpolarized gas functional lung imaging.

The original counter-flow xenon polarizer prototype [3] developed at UNH and presently installed at the Brigham and Women's Hospital (BWH), Boston, MA, utilizes a uniform polarizing field generated by seven coils 1.1 m in diameter with ancillary subsystems located outside the fringe field. It requires operator attention every two minutes to adjust the level of the cryogen to optimize the freeze-out.

Xemed has reduced the polarizer size and automated its operation (Figure 3):

1. The uniform polarizing magnetic field and the high uniformity NMR region are now isolated from the high-strength freezeout magnet. This demanded an innovative structured permeability design and precise implementation.
2. The freezeout/thaw system has been increased in capacity and its operation has been automated.
3. The laser has been reduced in size and cost, and equipped with an external cavity [4].

In Figure 3, a shield cage, which also functions as a return yoke, has been removed to show the 1.6-meter long polarization column and 16-coil solenoid tower mounted inside. A laser beam enters from the top via a periscope and is directed down via a 45° dielectric mirror. Xenon gas enters from the bottom of the column, flows opposite to the direction of the laser beam through a 54mm diameter polarization chamber, and exits at the top into the permanent magnet subsystem. It consists of a field rotator, a uniform field for NMR measurement, and a 4 kGauss freezeout region. The NMR operates at 83 gauss for xenon and 23 gauss for proton calibration with uniformity of 10^{-4}.

Future Development

A new 6” square copper prototype is being developed to demonstrate order-of-magnitude scale-up of xenon polarization. It has recently been tested at low power, demonstrating a factor of five enhancement in output over our previous data, yielding 5.5 L/hr at 54% polarization. Development and scale-up of this polarizer is ongoing.

Breathing Protocol for ^{129}Xe and Safety issues

The early design UNH polarizer was installed at BWH and became operational in the second quarter of 2005. This polarizer has produced 1-2 L of ^{129}Xe per hour at ~55% polarization and has had very little down time. All studies were conducted in accordance with IRB and FDA IND approved protocols and informed consent was obtained as a prerequisite for participation. The protocol requires all inhaled gas mixtures to contain at least 21% oxygen and no more than 70% xenon. In addition, the estimated alveolar xenon concentration can be no more than 35%, which is well below the level (~70%) that induces anesthesia [5]. Standard pulmonary function tests were performed on each subject to obtain their residual volume (RV) and total lung capacity (TLC). These values were used to calculate the volume of oxygen and air needed for a particular volume of xenon in order to satisfy the protocol. Breath hold times are limited to 40 s for healthy subjects and 20 s for those with mild to moderate lung disease. Baseline measurements of the saturation of peripheral blood oxygen (SpO2), ECG, blood pressure, heart rate, and respiratory rate are measured for each subject before beginning a series of experiments

and 10 minutes after each breath hold experiment. SpO2 and heart rate are also monitored while in the MRI scanner. Several practice sessions are performed outside the scanner, some with air and one with a volume of natural xenon equal to the maximum amount of ^{129}Xe that would be used for any of the experiments planned for that particular subject. The practice breaths familiarize the subject with the protocol and allow them to experience what breathing ^{129}Xe will be like. We also check to make sure the SpO2 stays within allowed limits: no lower than an absolute value of 85% for healthy subjects. To date, 26 subjects have participated in various experiments involving at least 350 xenon breath hold tests. Three of the 26 subjects have mild interstitial lung disease and performed 32 breath hold experiments. The remainder of the experiments included only healthy subjects. There have been no adverse events. Before breathing xenon, a subject is instructed to perform 2 cycles of a deep breath to TLC followed by exhalation to close to RV. These vital capacity maneuvers are done to standardize the volume history for each subject.

For 5 of the 26 subjects, the number of breath hold experiments is ≥ 18 and for these five subjects, we compiled the mean, standard deviation and *p* value using a two tailed, paired *t*-Test to determine if there was a statistically significant difference in blood pressure or SpO2 from baseline, which was usually recorded at the beginning of the day, to measurements made 10 minutes after each experiment. Note that because of the ~1 hr time required to polarize a sufficient volume of xenon gas for an experiment (typically 1 – 2 liters), the time interval between experiments was at least 1 hr and typically 1.5 hrs. Thus, while a single breath hold experiment is very short (10 – 40 s), different experiments for a single subject typically occurred at multiple time points over a period of many hours. Table 1 lists results of the statistical analysis and Figure 4 shows typical blood pressure data for one subject, HS4, who over a 26 month period, performed 103 breath hold experiments. As expected, the mean values for all parameters changed by a very small amount. For subjects 4, 6, 13, 22, and 15, the percent changes from baseline to a measurement 10 minutes after a breath hold of xenon for systolic blood pressure, diastolic blood pressure, and SpO2 are shown in Table 2. Note that despite the fact that for some measurements $p<0.05$ (see Table 1), there is no general trend. Further, since we did not control for physical activity (including whether the subject had something to drink or eat) in the time intervals between the baseline measurement and those acquired 10 minutes after each experiment, any of the observed changes could easily be due to normal physiological variation.

The lack of adverse events as well as the fact that there was no significant effect on the parameters we measured is not surprising, especially in light of the fact that a different isotope of xenon has been used safely for many years to measure cerebral blood flow with CT. For example, Latchaw et al [5] reviewed adverse reactions for xenon CT in a multi-center study involving 1,830 patients and concluded that the side effects of xenon gas are minimal when its percentage concentration in the gas inhaled is less than 32%. Note that xenon CT typically involves continuous breathing of xenon for 5 minutes whereas our MRI protocol calls for a single breath repeated at most once every 5 minutes. In addition, in initial studies with hyperpolarized ^{129}Xe MRI, Mugler et al [6,7] reported only occasional lightheadedness, dry mouth and mild throat irritation when subjects inhaled 500 cc of laser polarized ^{129}Xe. Occasional light-headedness was also observed by Yonas et al [8] in their xenon CT studies.

Despite the xenon CT data indicating the safety of breathing xenon, regulatory agencies have been concerned that the gas, as prepared by a laser polarizer, is safe. Xenon CT studies do not use hyperpolarized xenon. Therefore, we feel it is important to report the results above, even if to indicate that there have been no significant measurable effects from our protocol.

MRI Hardware

All experiments were performed on a GE Signa Profile IV MRI magnet (0.2 T) interfaced with a broadband Tecmag Apollo (Houston, Texas) research console. A Mirtech, Inc (Brockton, MA) whole body transmit/receive coil, with an unloaded Q=300, operating at ^{129}Xe frequency (2.361 MHz) was used for all ^{129}Xe lung studies.

Alveolar surface area measurements with ^{129}Xe

In 2002, using a Chemical Shift Saturation Recovery (CSSR) method [9], we demonstrated the ability to measure surface area per unit gas volume S/V_{gas} in porous polyethylene phantoms by comparing our magnetic resonance results with confocal microscopy measurements of the mean chord length. Our initial results in humans at 0.2 T [10,11], summarized below, are promising; however, they have yet to be compared with gold standard histology measurements in animals. Since emphysema is known to cause loss of alveolar surface area S_A through septal wall destruction, S_A/V_{gas} is an important quantity since it directly measures the functional parameter associated with this disease.

CSSR involves the selective saturation of ^{129}Xe magnetization in the dissolved phase (i.e. in septal tissue) followed by the measurement of its recovery by diffusion of hyperpolarized ^{129}Xe from the alveolar gas spaces to septal tissue. A similar method has been used in animals by several other investigators [12-15]. Mansson et al [14] have shown that by solving the 1D diffusion equation and fitting their data to this model, one can obtain quantitative information about the thickness of both the parenchymal and blood compartments as well as information about perfusion. Driehuys [15] has shown that by observing time delays in the appearance of the spectral peak associated with the blood, one can determine the thickness of the parenchymal layer, separating gas and blood compartments, thereby identifying thickening to due interstitial disease.

In our work, Butler et al [9] showed that for a semi-infinite medium (see Figure 5a), the fraction $F(t)$ of the ^{129}Xe magnetization that has diffused into the dissolved phase after a diffusion time t relative to the initial, t=0, ^{129}Xe magnetization that was available in the gas phase is proportional to S_A/V_{gas}:

$$F(t) = \frac{\int s_{diss}(t,\omega)\, d\omega}{\int s_{gas}(t=0,\omega)\, d\omega} = \lambda \frac{S_A}{V_{gas}} \sqrt{\frac{4D_{diss}t}{\pi}} \qquad [1]$$

Here, the integrals are over the spectral width of the dissolved s_{diss} and gas s_{gas} signals, λ is the Ostwald solubility coefficient, and D_{diss} is the diffusivity of ^{129}Xe in the dissolved phase. V_{gas} is the gas volume and S_A is the alveolar surface area between the two phases. We recently reported CSSR results in healthy humans [10,11] and a typical example is shown in Figure 6. For an ideal semi-infinite medium (Figure 5a), the dissolved state signal increases diffusively as $\sqrt{t}$ for all times t. However, the thickness of septal tissue is not infinite, and thus saturates at long times (Figure 5b). The red line in Figure 6 shows a fit of $F(t)$ to $\sqrt{t}$ for the early time data before the septa are saturated. Measurements with four healthy subjects at multiple lung volumes [11] showed that the slope of F with respect to $\sqrt{t}$ can be measured with an average error bar of 13%. Using literature values for λ~0.1 [16] and D_{diss} ~3×10^{-6} cm^2/s [17], one can compute S_A/V_{gas}. Note that to obtain good fits to the CSSR data, the $\sqrt{t}$ fits also include a DC offset term. We believe this is because our earliest diffusion time in a CSSR experiment is 17 ms, during which one estimates ^{129}Xe diffuses within the parenchyma by ~3 μm, thereby saturating the thinner, connective tissue portions of the septa. These thinner regions remain saturated at all longer diffusion times and therefore appear as a DC offset. Thus, the diffusion we are observing within the $\sqrt{t}$ early times of our data most likely corresponds to the thicker portions of the septa occupied by capillaries. Therefore, we expect our CSSR values of S_A/

V_{gas} to be smaller than those obtained from histology. A comparison [11] shows that our values are ~40% lower than those obtained from fixed lung morphometry.

The minimum diffusion time is strongly influenced by the length of the chemically selective RF pulse that saturates the dissolved phase. At 0.2 T, the difference between the dissolved and gas phase resonance is ~205 ppm, which corresponds to ~500 Hz. To produce a highly selective RF pulse, we used a 10 ms long trapezoidally shaped pulse [18]. At higher field strength, where the absolute frequency difference between dissolved and gas phases is larger, smaller minimum diffusion times should be possible.

Single-Breath XTC (SB-XTC)

The signal-to-noise ratio (SNR) of CSSR is insufficient for imaging [11]. Therefore, we adapted the xenon transfer contrast (XTC) method developed by Ruppert et al [12,13]. XTC measures the diffusion into the dissolved phase indirectly by looking at the attenuation in the gas phase signal after multiple opportunities for interphase diffusion. Ruppert et al's implementation of XTC involves two separate breath hold experiments. One experiment, the control experiment, measures the voxel by voxel attenuation due to two “unwanted” sources of attenuation, i.e. T_1 decay due to the presence of oxygen (discussed below) and depletion of the ^{129}Xe magnetization reservoir due to the RF pulses used for imaging. A second XTC experiment measures the attenuation from the two “unwanted” sources as well as that due to interphase diffusion. The interphase diffusion part can then be solved for by using the results from the control experiment to remove the “unwanted” sources of attenuation in the XTC experiment. As originally implemented, XTC is a two breath hold protocol. We modified the technique to a single breath (SB-XTC) method [10,11,18]. Typical examples of data obtained at two different lung volumes with SB-XTC from a subject (HS6) in the supine position are shown in Figures 7 and 8. Imaging parameters here are identical to those reported by Muradian et al [18] (matrix 64 (readout) × 32 (phase encode), pixel size 4.69mm × 9.38mm, TE/TR = 5.23/28.47ms, FOV=300mm, readout bandwidth = ±2893.5Hz). The echo was asymmetric and was refocused 20% through the readout time. The diffusion time τ =62 ms and was chosen to lie well within the early time regime, i.e. F linear with $\sqrt{t}$, that was measured with CSSR. For reconstruction, the data was zero filled to 128 × 128. After FT and magnitude calculation, signal below 10% of the maximum was masked.

Figures 7 and 8 show SB-XTC data from two different lung volumes. Subfigures (a-c) show the three acquired SB-XTC images, from which a map of F_{XTC} is calculated, as shown in (d). The histogram for (d) is shown in (f). Figure 9a shows $<F_{XTC}>$ (averaged right/left) as function of superior/inferior position. Note that there is a superior/inferior gradient in $<F_{XTC}>$ for the lower lung volume (Figure 7, 47% TLC) despite the fact that the subject is supine. In identical experiments acquired at a higher lung volume (Figure 8, 63% TLC), this gradient disappears. This behavior is consistent for a number of subjects [18] and believed to be due to a residual memory effect of being in the vertical position for a substantial portion of our lives. Closer to TLC, the lung is expected to be more homogeneous, which supports this observation that any residual gradient disappears at higher lung volumes.

An important question is whether or not F_{XTC} can be directly converted to S_A/V_{gas} in a similar manner as F_{CSSR}. There are two issues here: First, what is the relationship between F_{XTC} and F_{CSSR}? Ruppert et al [13] argue that for very long interphase diffusion times τ, $F_{XTC}(\tau) = 2F_{CSSR}(\tau)$. In a direct comparison, we performed whole lung spectroscopic measurements of both F_{XTC} and F_{CSSR} vs t on the same subject under identical conditions [11]. This very preliminary data shows $K_{XTC} / K_{CSSR} = 2.52 \pm 0.17$, where K is the slope of F vs $\sqrt{t}$. Second, to calculate S_A/V_{gas}, we use the slope K_{CSSR} and Equation [1] to convert to S_A/V_{gas}. For SB-XTC, we acquire data at a single time point, and since there is a DC offset in the F vs t data,

one cannot accurately determine the slope. This means that absolute determinations of S_A/V_{gas} from the single time point SB-XTC data are not possible. On the other hand, relative values of F_{XTC} will accurately reflect relative values of S_A/V_{gas} if the conversion factor between K_{CSSR} and K_{XTC} is known.

Measurement of pO_2

Hyperpolarized gases utilizing either ^{129}Xe or ^{3}He are sensitive to intrapulmonary oxygen partial pressures (pO_2). Prior to hyperpolarized gas studies, pO_2 could only be measured by invasive means. Variation in regional pO_2 results from differences in ventilation-dependent delivery of O_2 to the aveoli and the perfusion-dependent uptake by venous blood. Thus, regional pO_2 is an indicator of regional ventilation and perfusion matching. The basis for pO_2 measurements is that molecular oxygen shortens T_1. This is believed to occur primarily by way of intermolecular dipolar coupling between the electron spins of paramagnetic oxygen and the nuclear spin of the noble gas [19,20]. This interaction is normally expected to have a field/frequency dependent T_1 of the form:

$$\frac{1}{T_1}=\frac{pO_2}{\xi}=\frac{pO_2}{\xi_o(T)}\left(1-f(T)\,\omega^{1/2}\right), \quad [2]$$

where pO_2 is the oxygen partial pressure (in bars), T is the temperature in degrees Kelvin, ω is the Larmor frequency (rad/s), and ξ and f are temperature dependent coefficients. We refer to ξ as the Oxygen Enhancement Factor (OEF), i.e. increasing OEF increases T_1. A small frequency dependence for the OEF has been observed for ^{129}Xe [19]. Even though there are no experimental measurements of the field dependence for ^{3}He relaxation with oxygen, theoretical considerations (based upon He appearing to be a harder sphere than Xe) suggest that there may be none [20]. For convenience, the OEF (calculated from [19,20]) is presented in Table 3 for different temperatures (room and physiological temperatures) for both nuclei and at different field strengths for ^{129}Xe. For example, if one assumes an alveolar pO_2 of 100mm Hg (0.13 bar), T_1 at 0.2T and 37° C is 19s.

Table 3 shows that the temperature and field strength variations can easily provide ~20% variation for the xenon relaxation rate. Though the temperature difference between room temperature and physiological temperature is small, it should be considered when comparing data from phantom measurements to *in vivo* studies. Recent measurements (not shown) by us at 0.2 T on hyperpolarized ^{129}Xe gas samples at room temperature confirm to within 4% the expected relaxation rate given in Table 3.

In the case of ^{3}He, careful regional measurements of T_1 allow for quantitative regional pO_2 determinations [21-26]. A complicating factor for 2D slice techniques is the diffusion of helium between slices [25]. A single scan 3D method, however, seems to alleviate this problem [26]. It has also been reported that even slight variations of pO_2 due to apnea during a single breath hold can be measured [22,23].

The recent advances in hyperpolarized ^{129}Xe production described above have allowed us to extend these measurements to ^{129}Xe in healthy volunteers. Recent results [27] utilizing constant flip angles and spectroscopic data from whole lung experiments reveal the typical exponential decay after correcting for the decay component of the signal due to RF pulses. However, we obtain much higher estimates of pO_2 (~40% higher) than expected. Unlike helium, xenon has a finite solubility in parenchymal tissue [16] and this leads to an additional decay of the gas signal that needs to be accounted for in order to accurately measure T_1. From estimates of typical pO_2 levels at RV and the known inspired volume of oxygen in a normal healthy lung, it is possible to subtract off the contribution of oxygen to the relaxation rate. This provides an estimated value of T_1 due to ^{129}Xe gas interphase exchange: $T_{1,exch}$~35s [27].

Therefore, if the actual T_1 due to the presence of oxygen in the lung is $T_{1,O2}$= 19s, then this additional decay mechanism due to xenon interphase exchange into tissue causes one to measure an effective T_1 of $T_{1,\text{meas}}$=12.3s, i.e. $1/T_{1,meas} = 1/T_{1,exch} + 1/T_{1,O2}$. Therefore, if we do not correct for the effects of diffusion of xenon into the septal tissue, the pO_2 that we calculate is the *equivalent* pO_2 (pO_2-equiv) that would cause the same relaxation by itself as is observed from both the actual pO_2 as well as that due to diffusion into tissue. Thus, using the first two gradient echo images acquired serially from our SB-XTC protocol, we computed pO_2-equiv. Figures 7 and 8 (e and g) show the results for the pO_2-equiv maps and their histograms respectively for two different lung volumes. Figure 9b shows the <pO_2-equiv> (averaged right/left) as a function of superior/inferior position.

Discussion of pO_2-equiv Results

In the upright position, both ventilation and perfusion are higher in the base than in the apex. However, perfusion has a much steeper gradient than ventilation and therefore V/Q is higher at the apex than in the base, accounting for a pO_2 shift from ~170 mbar (~130 torr) at the apex compared to 120 mbar (90 torr) at the base [28]. Note that this gradient, higher pO_2 at the apex is opposite that for $<F_{XTC}>$ that we see at lower lung volumes, i.e. higher $<F_{XTC}>$ at the base. If a gradient in $<F_{XTC}>$ exists, we expect that this will induce a change in pO_2 in the opposite direction because an increase in $<F_{XTC}>$ corresponds to higher S_A/V_{gas}, which will cause an increase in gas exchange and a reduction in pO_2 in the alveolar gas spaces. In the supine position, the perfusion gradient due to gravity disappears and one expects a very mild V/Q gradient and therefore almost no change in pO_2. At the higher lung volume (Figure 8) of 63% of TLC, there is essentially no gradient in $<F_{XTC}>$ from base to apex. Therefore, because these two components that make up pO_2-equiv are relatively constant from base to apex, we expect the experimental measurement (Figure 9b) to also reflect this. What we observe in Fig. 9b is a weak gradient where pO_2-equiv is ~15% higher at the base. However, as one goes to lower lung volume (47% TLC), we now observe a gradient in $<F_{XTC}>$ where $<F_{XTC}>$ at the base is higher than at the apex. That should induce an oppositely directed gradient in pO_2, i.e. lower pO_2 at the base compared to the apex and that is exactly what the data shows.

Intrapulmonary pO_2 clearly affects both xenon and helium relaxation rates. At this time, however, for the measurement of pO_2 only, ^{3}He has an advantage since it is not complicated by exchange with parenchymal tissue. Furthermore, the expected lack of field dependence and smaller temperature variation for ^{3}He OEF, simplifies measurements of intrapulmonary pO_2. On the other hand, ^{129}Xe consistently overestimates pO_2 levels and it is for this reason that pO_2 maps for xenon should be referred to as pO_2-equiv maps. Despite the fact that pO_2-equiv maps do not give correct absolute values of pO_2, when combined with F_{XTC} maps and different lung volume measurements, important functional information can be inferred.

Conclusions

We have reviewed the history of hyperpolarized ^{129}Xe gas production and described the novel counter-flow polarizer that has enabled high magnetization throughput. In addition, we have described improvements on the initial design, where the operation is more automated and the overall size has been reduced to the size of a single equipment rack. We have reported our progress towards a new polarizer design for an order of magnitude improvement in magnetization throughput. We are very encouraged by our recent demonstration of 54% polarization at a production rate of 5.5 liters/hour. We have also reported detailed statistics for both blood pressure and SpO2 before and after breathing ^{129}Xe in our protocol and concluded that there are no significant physiological effects. We have summarized prior results demonstrating the measurement of S_A/V_{gas}. Whole lung CSSR data are easily quantifiable, although with limited signal to noise ratio. This has led us to adapt the XTC method for imaging

F. We have described lung volume dependent changes in the apex/base gradient of $<F_{XTC}>$. We have reported our measurements of what we call pO_2-equivalent. This corresponds to the equivalent pO_2 that would cause the observed decay between two serially acquired gradient echo images that is due not only to pO_2 but also due to interphase exchange of ^{129}Xe. We demonstrated that the apex to base pO_2-equiv gradient reverses direction with lung volume and that this corresponds to expected behavior based on the observation of the changes in $<F_{XTC}>$.

Based on the measurements reported here as well as those of others [29] that demonstrate comparable apparent diffusion coefficient ADC sensitivity of ^{129}Xe to the well established results with ^{3}He, we conclude that the there is great promise for ^{129}Xe as a pulmonary functional imaging modality.

Acknowledgements

Grant Support: NIH RO1 HL73632, RR14297, HL67784, EB02553,RR20200, HL78285, HL82013, ES14005, HL87550

References

1. Hyperpolarized Gas Study Group Meeting. ISMRM Fifteenth Scientific Meeting; Berlin. 2007.
2. Hersman, FW.; Leuschner, M.; Carberry, J. Apparatus and methods for polarizing polarizable nuclear species. US Patent 6,949,169. 2005. issued September 27
3. Ruset IC, Ketel S, Hersman FW. Optical pumping system design for large production of hyperpolarized. Phys Rev Lett 2006;96(5)053002 Epub 2006 Feb 9
4. Zhu H, Ruset IC, Hersman FW. Optics Letters 2005;30(11):1342–1344. [PubMed: 15981527]
5. Latchaw RE, Yonas H, Pentheny SL, Gur D. CT cerebral blood flow determination. Radiology 1987;163:251–254. [PubMed: 3823444]
6. Mugler JP, Driehuys B, Brookeman JR, et al. MR Imaging and Spectroscopy Using Hyperpolarized ^{129}Xe Gas: Preliminary Human Results. Magn Reson Med 1997;37(6):809–815. [PubMed: 9178229]
7. Mugler JP, Mata JF, Wang H-TJ, et al. The Apparent Diffusion Coefficient of Xe-^{129} in the Lung: Preliminary Results. Proc 11th Intl Soc Magn Reson Med 2004:769.
8. Yonas H, Grundy B, Gur D, Shabason L, Wolfson SK, Cook EE. Side Effects of xenon inhalation. J Comput Assist Tomogr 1981;5(4):591–592. [PubMed: 7264006]
9. Butler JP, Mair RW, Hoffmann D, et al. Measuring Surface-Area-to-Volume Ratios in Soft Porous Materials using Laser-Polarized Xenon Interphase Exchange NMR. J Phys Condens 2002;14 (13):L297–304.
10. Patz, S.; Muradian, I.; Hrovat, MI., et al. Hyperpolarized ^{129}Xe Human Gas Exchange at 0.2T with XTC; 14th Annual Intl Soc Magn Reson Med; Seattle. May 2006; p. 192
11. Patz S, Muradian I, Hrovat MI, et al. Human Pulmonary Imaging and Spectroscopy with Hyperpolarized 129Xe at 0.2T. Acad Radiol. submitted
12. Ruppert K, Brookeman JR, Hagspiel KD, Mugler JP III. Probing lung physiology with xenon polarization transfer contrast (XTC). Magn Reson Med 2000;44(3):349–357. [PubMed: 10975884]
13. Ruppert K, Mata JF, Brookeman JR, Hagspiel KD, Mugler JP III. Exploring lung function with hyperpolarized ^{129}Xe nuclear magnetic resonance. Magn Reson Med 2004;51(4):676–687. [PubMed: 15065239]
14. Mansson S, Wolber J, Driehuys B, et al. Characterization of Diffusing Capacity and Perfusion of the Rat Lung in a Lipopolysaccaride Disease Model Using Hyperpolarized ^{129}Xe. Magn Reson Med 2003;50(6):1170–1179. [PubMed: 14648564]
15. Driehuys B, Cofer GP, Pollaro J, et al. Imaging alveolar-capillary gas transfer using hyperpolarized ^{129}Xe MRI. PNAS 2006;103(48):18278–18283. [PubMed: 17101964]
16. Eger EL, Larson CP. Anaesthetic Solubility in Blood and Tissues: Values And Significance. Brit J Anaesth 1964;36:140–144. [PubMed: 14164257]

17. Sta MN, Eckmann DM. Model Predictions of Gas Embolism Growth and Reabsorption during Xenon Anesthesia. Anesthesiology 2003;99(3):638–645. [PubMed: 12960548]

18. Muradian I, Butler JP, Hrovat M, et al. Human Pulmonary Gas Exchange with Xenon Polarization Transfer Contrast (XTC). Magn Reson Med. 2007in press

19. Jameson CJ, Jameson AK, Hwang JK. Nuclear spin relaxation by intermolecular magnetic dipole coupling in the gas phase. ^{129}Xe in oxygen. J Chem Phys 1988;89(7):4074–4081.

20. Saam B, Happer W, Middleton H. Nuclear relaxation of ^{3}He in the presence of O_2. Phys Rev A 1995;52(1):862–865. [PubMed: 9912313]

21. Eberle B, Weiler N, Markstaller K, et al. Analysis of intrapulmonary O_2 concentration by MR imaging of inhaled hyperpolarized helium-3. J Appl Physiol 1999;87(6):2043–2052. [PubMed: 10601148]

22. Deninger AJ, Eberle B, Ebert M, et al. Quantification of Regional Intrapulmonary Oxygen Partial Pressure Evolution during Apnea by ^{3}He MRI. J Magn Res 1999;141(2):207–216.

23. Deninger AJ, Eberle B, Ebert M, et al. ^{3}He-MRI-based measurements of intrapulmonary pO_2 and its time course during apnea in healthy volunteers: first results, reproducibility, and technical limitations. NMR Biomed 2000;13(4):194–201. [PubMed: 10867696]

24. Deninger AJ, Eberle B, Bermuth J, et al. Assessment of a Single-Acquisition Imaging Sequence for Oxygen-Sensitive ^{3}He-MRI. Magn Reson Med 2002;47(1):105–114. [PubMed: 11754449]

25. Wild JM, Fichele S, Woodhouse N, Paley MN, Kasuboski L, van Beek EJ. 3D volume-localized pO2 measurement in the human lung with 3He MRI. Magn Reson Med 2005;53(5):1055–64. [PubMed: 15844148]

26. Wild JM, Teh K, Woodhouse N, et al. Single Scan 3D pO_2 Mapping with Hyperpolarized 3He MRI. ISMRM 2006;14:869.

27. Hrovat MI, Muradyan I, Ketel S, et al. Human Pulmonary pO_2 at 0.2T with Hyperpolarized 129Xe. ISMRM 2006;14:1305.

28. West, JB. The Essentials. Sixth Edition. Williams & Wilkins; Lippincott: 2000. Respiratory Physiology.

29. Mata JF, Altes TA, Cai J, et al. Evaluation of emphysema severity and progression in a rabbit model: comparison of hyperpolarized 3He and 129Xe diffusion MRI with lung morphometry. J Appl Physiol 2007;102(3):1273–80. [PubMed: 17110518]

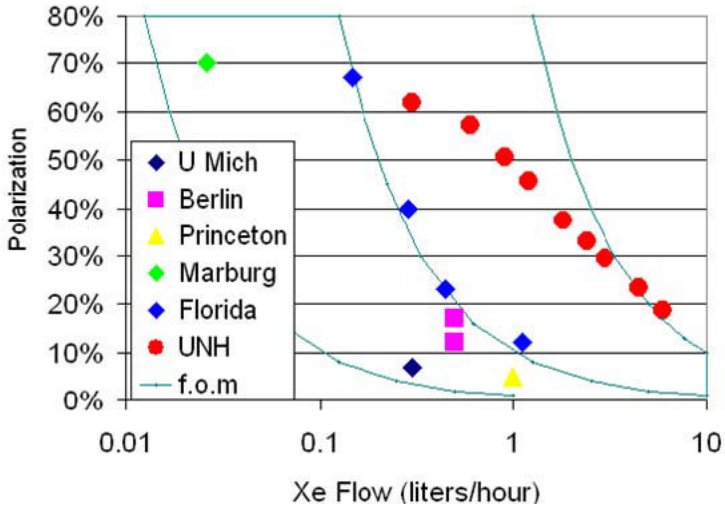

Figure 1.
Polarization is plotted against output rate for the UNH polarizer and several other polarization technologies. Highest magnetization, indicated by the figure-of-merit contours, is available at lowest values of polarization.

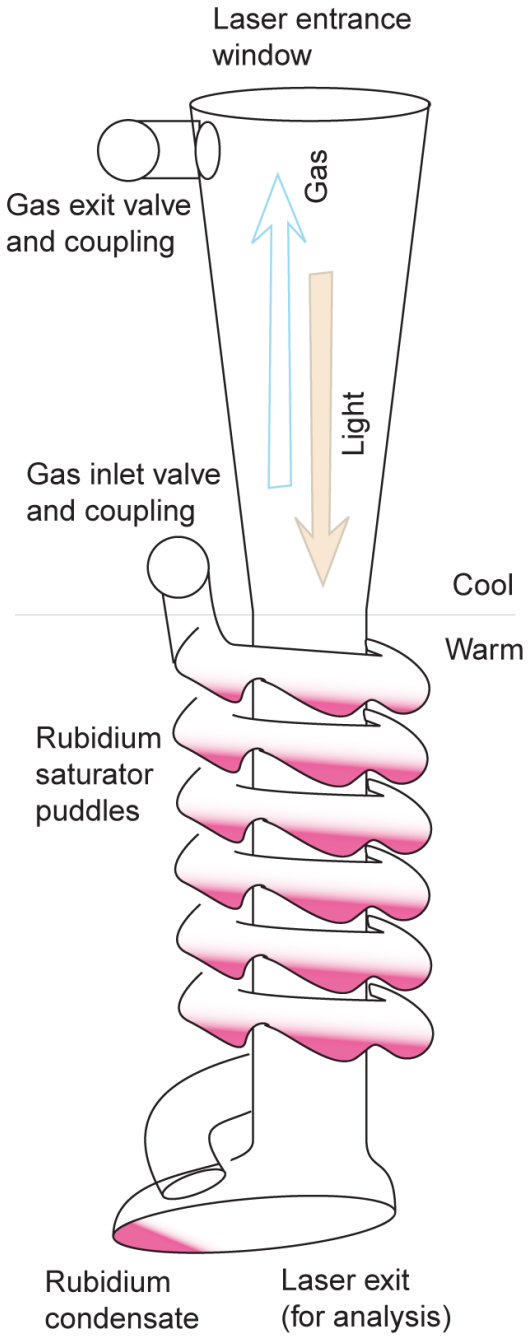

Figure 2.
The laser light enters the polarization column along a ***direction opposite the flow of gas***

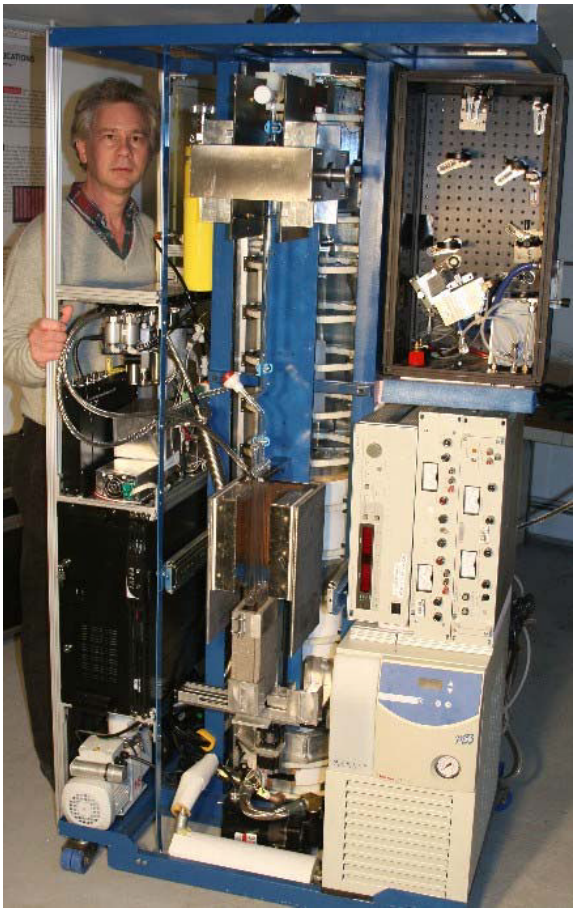

Figure 3.
Prof Hersman with Xemed's compact clinical HXe polarizer “Bell” in January 2007.

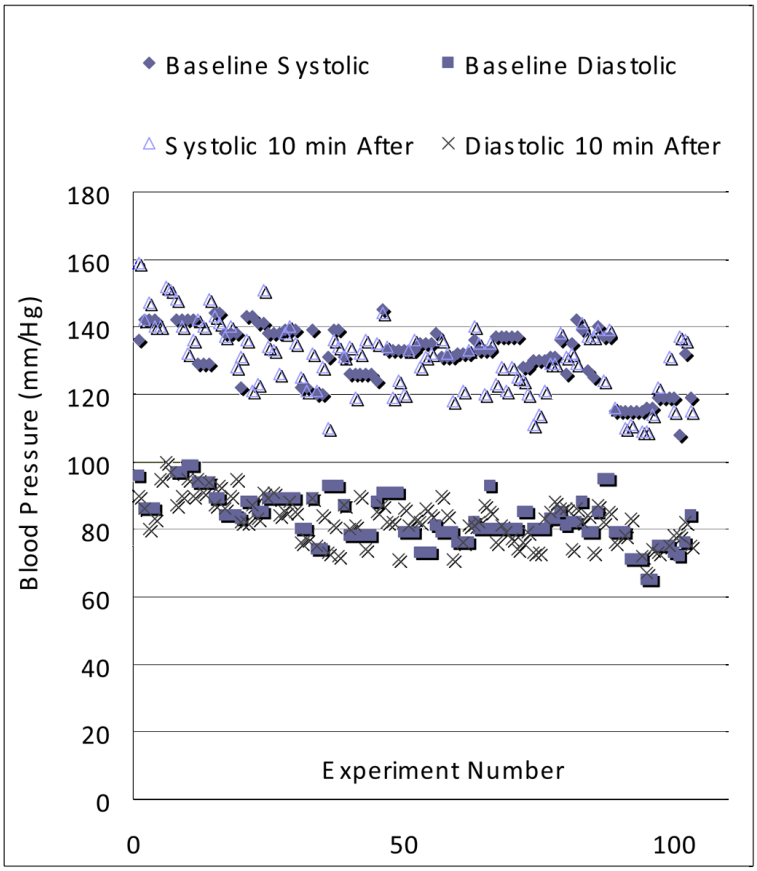

Figure 4.
Blood pressure at baseline and 10 minutes after each breath hold experiment for human subject 4 (HS4). This data was acquired from 5/4/2005 to 7/14/2007.

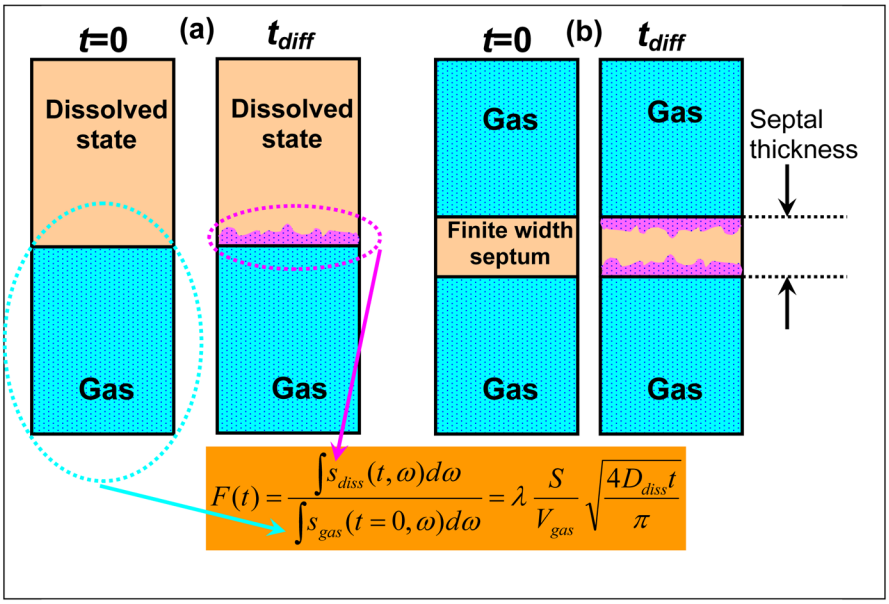

Figure 5.
Schematic of Chemical Shift Saturation Recovery method. (a) Idealized 1D semi-infinite phases. (b) A more realistic model with a finite width septum. Net diffusion from gas to dissolved phase after time t_{diff} is shown in purple.

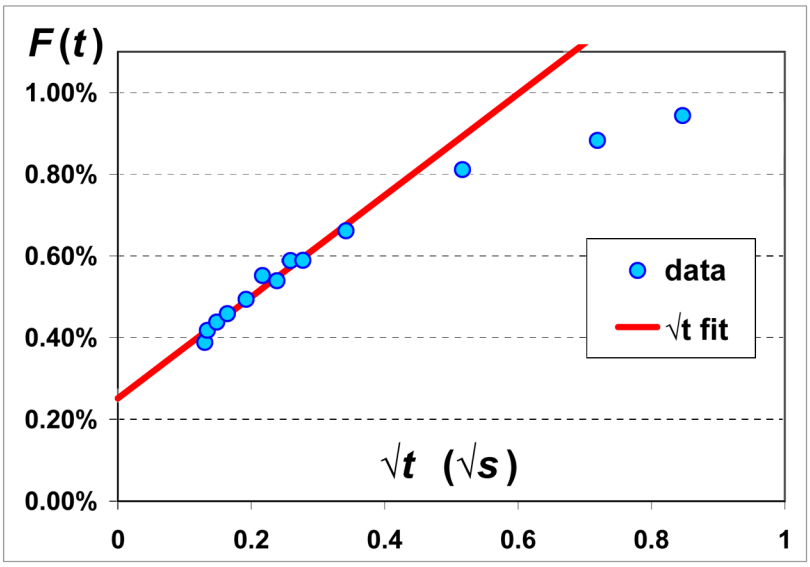

Figure 6.
Experimentally measured $F(t)$ shown with blue dots as a function of $\sqrt{t}$. Lung volume was fixed and in the example shown here, it is at total lung capacity (TLC). Also shown is a fit to the early time data using Eqn [1] (red line).

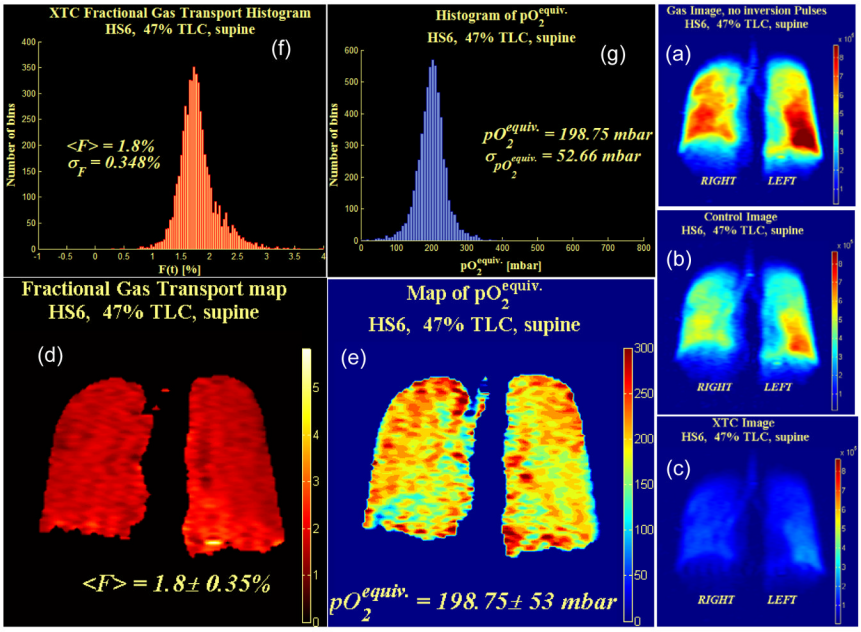

Figure 7. SB-XTC raw and processed data

Coronal projection images were acquired from subject HS6 in the supine position after 1L of 86% enriched ^{129}Xe was inhaled (47% TLC). (a-c) Example of the three serially acquired single breath XTC (SB-XTC) gradient echo images and the information obtained from them. (a) First image showing ^{129}Xe ventilation, (b) second "control" image that was acquired after image (a) and then an XTC exchange sensitization (RF pulses off resonance) so that the only attenuation between image (a) and (b) is due to RF depletion and T_1 decay from pO_2, (c) third "XTC" image acquired after image (b) and an XTC exchange sensitization (RF pulses applied on resonance) so that the attenuation between image (b) and (c) is due to RF depletion, T_1 decay from pO_2, and ^{129}Xe interphase diffusion. Voxels in image (c) have been scaled up by the attenuation factor measured between (a) and (b) so that the attenuation observed between (b) and (c) is solely due to interphase diffusion. Also shown are (d) the resulting F_{XTC} and (e) pO_2-equiv maps, and their respective histograms (f) and (g).

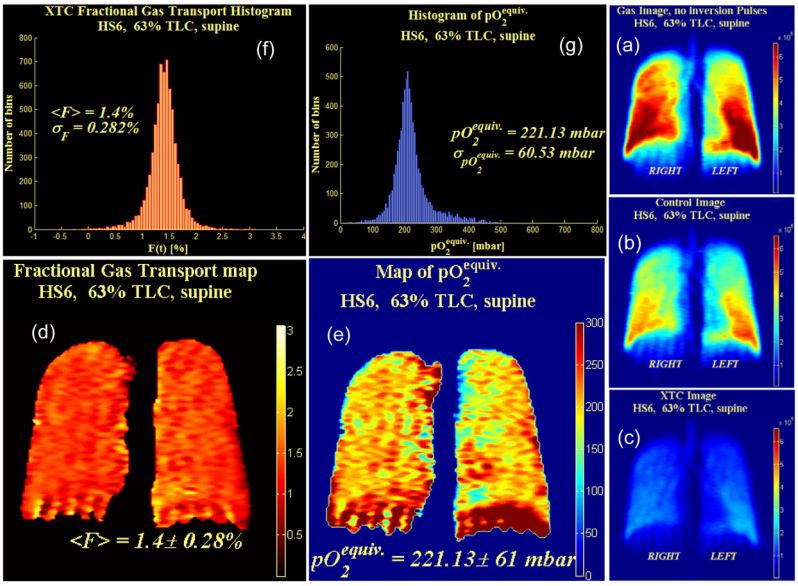

Figure 8. SB-XTC raw and processed data

Coronal projection images were acquired from subject HS6 in the supine position after 1.8L of 86% enriched ^{129}Xe was inhaled (63% TLC). Description for subfigures a-g is identical to Figure 7.

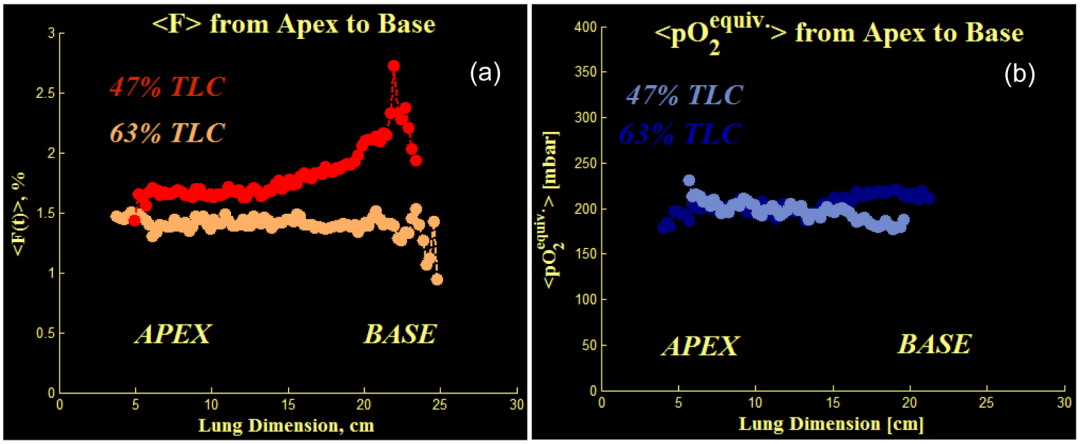

Figure 9.

Comparison of apex to base (a) $<F_{XTC}>$ and (b) $<pO_2$-equiv> averaged right/left as a function of apex to base (superior to inferior) position. Note that the region in the immediate vicinity of the diaphragm for the $<pO_2$-equiv> plot at 63% lung volume was inconsistent with the remainder of the lung. Artifacts due to diaphragm motion are suspected to be the cause. This region was excluded from the plot below because of excessive variability of $<pO_2$-equiv> in that region.

Table 1

Blood Pressure (BP) and SpO_2 statistics for subjects who had 18 or more breath hold experiments. The *p* values are computed for a two-tailed paired distribution.

Subject	Number of expts	Systolic BP Baseline mean	Systolic BP 10 min after mean	*p* value	Diastolic BP Baseline mean	Diastolic BP 10 min after	*p* value	SpO2 Baseline mean	SpO2 10 min after mean	*p* value
4	103	131.6 ±8.6	130.8 ±10.6	0.051	83.0 ±7.4	82.8 6.7	0.155	98.1 ±1.1	97.6 ±1.2	3×10^{-4}
6	60	117.9 ±4.7	118.7 ±6.6	0.38	76.0 ±4.7	79.2 ±6.4	0.001	97.8 ±0.8	97.6±0.9	0.26
13	33	126.6 ±9.3	128.7 ±6.9	0.175	73.0 ±5.1	77.0 ±4.8	1×10^{-4}	98.0 ±1.1	97.6 ±0.7	0.23
22	19	118.9 ±6.6	118.3 ±8.6	0.94	62.9 ±2.7	65.1 ±5.7	0.16	97.5 ±0.5	97.2 ±0.7	0.096
15	18	112.4 ±6.6	118.3 ±6.7	0.041	69.3 ±3.2	68.9 ±4.1	0.43	97.8 ±1.2	97.0 ±1.0	0.060

Table 2

Average Percent Change in blood pressure and SpO_2 from baseline measurements before breathing ^{129}Xe to 10 min after each breath hold.

Subject	Before/After % Change		
	Systolic B	Diastolic BP	SpO2
4	−0.60	−0.24	−0.51
6	+0.68	+4.10	−0.20
13	+1.65	+1.53	−0.41
22	−0.51	+3.40	−0.31
15	+5.10	−0.57	−0.82

Table 3

Oxygen Enhancement Factor

Field Strength	T(K)	ξ (bar s)	T(K)	ξ (bar s)
^{129}Xe				
0.2T	295	2.31	310	2.51
1.5T	295	2.52	310	2.72
3.0T	295	2.68	310	2.88
^{3}He				
1.4T	295	2.42	310	2.59*

* Deninger [21] reports a value of 2.61